# Metamagnetic texture in a polar antiferromagnet

D. A. Sokolov [1]*, N. Kikugawa[2], T. Helm[1], H. Borrmann[1], U. Burkhardt[1], R. Cubitt [3], J. S. White [4], E. Ressouche[5], M. Bleuel[6,7], K. Kummer[8], A. P. Mackenzie[1,9] and U. K. Rößler[10]

[1]Max Planck Institut für Chemische Physik fester Stoffe, Dresden, Germany. [2]National Institute for Materials Science, Tsukuba, Japan. [3]Institut Laue–Langevin, Grenoble, France. [4]Laboratory for Neutron Scattering and Imaging, Paul Scherrer Institute, Villigen, Switzerland. [5]Université Grenoble Alpes, CEA, INAC-MEM, Grenoble, France. [6]NIST Center for Neutron Research National Institute of Standards and Technology, Gaithersburg, MD, USA. [7]Department of Materials Science and Engineering, University of Maryland, College Park, MD, USA. [8]ESRF, Grenoble, France. [9]Scottish Universities Physics Alliance, School of Physics and Astronomy, University of St Andrews, St Andrews, UK. [10]Leibniz-Institut für Festkörper- und Werkstoffforschung, IFW, Dresden, Germany. *e-mail: dmitry.sokolov@cpfs.mpg.de

# Supplementary Information for Metamagnetic texture in a polar antiferromagnet

D. A. Sokolov,[1] N. Kikugawa,[2] T. Helm,[1] H. Borrmann,[1] U. Burkhardt,[1] R. Cubitt,[3] J. S. White,[4] E. Ressouche,[5] M. Bleuel,[6] K. Kummer,[7] A. P. Mackenzie,[1,8] and U.K. Rößler[9]

[1]*Max-Planck-Institut für Chemische Physik fester Stoffe, D-01187 Dresden, Germany*
[2]*National Institute for Materials Science, Tsukuba 305-0047, Japan*
[3]*Institut Laue-Langevin, 6 Rue Jules Horowitz, F-38042 Grenoble, France*
[4]*Laboratory for Neutron Scattering and Imaging (LNS),*
*Paul Scherrer Institute (PSI), CH-5232 Villigen, Switzerland*
[5]*Univ. Grenoble Alpes, CEA, INAC-MEM, 38000 Grenoble, France*
[6]*NIST Center for Neutron Research, NIST, Gaithersburg, MD 20899, USA*
[7]*ESRF, 71 avenue des Martyrs, 38000 Grenoble, France*
[8]*Scottish Universities Physics Alliance (SUPA), School of Physics and Astronomy,*
*University of St Andrews, St Andrews KY16 9SS, United Kingdom*
[9]*Leibniz-Institut für Festkörper- und Werkstoffforschung, IFW Dresden Germany*

## I. X-RAY MAGNETIC CIRCULAR DICHROISM (XMCD)

The X-ray magnetic circular dichroism (XMCD) experiment was performed at the ESRF beamline ID32 using the high-field magnet endstation[1]. The samples were cleaved in situ in the high field magnet at low temperature and a pressure better than $2 \times 10^{-10}$ mbar leaving behind a clean $ab$ surface. The magnetic field was applied along the beam direction. The $b$ axis of the samples was tilted by $15°$ towards the $c$ axis with respect to the field direction, resulting in a small field component along $c$ but zero field along $a$. The X-ray absorption spectra were taken in total electron yield mode with circular left and circular right polarization for both positive as well as negative field direction. The XMCD was determined from all four spectra as the difference between spectra taken with opposite helicity.

Fig. 1a shows the XAS spectra for positive and negative helicity and the XMCD obtained as the difference of the two in the CAFM phase at low temperature and high field. In addition to the Ru $M_3$ and $M_2$ absorption lines there is an additional broad X-ray absorption features around $450\,\text{eV}$ which displays no XMCD and is due to Ca $L_{3,2}$ absorption. We followed the XMCD signal at the Ru $M_{3,2}$ as a function of magnetic field and temperature in the relevant region of phase space. The obtained spectra are shown in Fig. 1b both with the relative intensities as measured (left panel) and with the intensities normalized to peak value (right panel). The intensity of the XMCD signal (left panel) scales well with the macroscopic magnetization curves shown in Fig. 2a of the manuscript. The lineshape of the XMCD, however, does not change, either with field or temperature, across the metamagnetic, magnetic and MIT transitions. Using the XMCD sum rules, we can extract the ratio of orbital to spin moment aligned along the field which only depends on the ratio of the integrated XMCD signal at the $M_3$ and $M_2$ absorption edge, respectively[2]. As the XMCD lineshape does not change across the phase diagram we always find the same value $< m_L > / < m_S > \approx 0.13 \pm 0.02$, confirming the presence of a sizable orbital moment. In principle, spin- and orbital moments can also be extracted individually from the XMCD signals[2]. We refrained from doing so here because of the complex background of the XAS spectra which makes it difficult to extract reliable numbers.

The robustness of the XMCD lineshape and the $< m_L > / < m_S >$ ratio suggests that the local crystal field experienced by the Ru ions in the $RuO_6$ octahedra does not change significantly in the interesting region of the phase diagram.

## II. TRANSPORT MEASUREMENTS

We carried out magnetotransport measurements on a sample in the Hall-bar geometry, prepared by focused Ion beam (FIB) microfabrication. A lamella with dimensions $(3 \times 20 \times 100)\ \mu\text{m}^3$ was cut from a single-crystal using Gallium FIB. The device is shown in the inset of Fig 2a. We used a standard four-terminal Lock-In method for measurements of electrical resistivity. We applied a current of 100 $\mu$A with frequency f = 177 Hz along the $a$-axis while the magnetic field was applied along the $b$ axis. The zero-field resistivity curve shown in Fig 2a resembles data reported previously[3] and demonstrates the high quality of micromachined devices. The in-plane resistivity, $\rho_{xx}$, as well as the Hall resistivity, $\rho_{yx}$, exhibit a step-like behavior at low temperatures (see Fig 2b and c). The sharp change evolves into a broader transition as temperature approaches 50 K. Above 50 K, both $\rho_{xx}$ and $\rho_{yx}$ follow an overall positive slope. Most interestingly, we observe a two-step-like behavior in $\rho_{yx}$ for temperatures between 45 K and 49 K, the range in which the metamagnetic texture was observed in small-angle neutron scattering measurements. In general, the Hall resistivity can be a composition of three components:

$$\rho_{yx} = \rho_{yx}^N + \rho_{yx}^A + \rho_{yx}^T, \tag{1}$$

where N, A, T denote the normal, anomalous and topological Hall effect contributions[4]. Using the expression:

$$\frac{\rho_{yx}}{H} = R_0 + \frac{S_A \rho_{xx}^\alpha M}{H} + \frac{\rho_{yx}^T}{H}, \tag{2}$$

where H is the magnetic field and M is the magnetization, we can extract the normal and anomalous Hall coefficients,
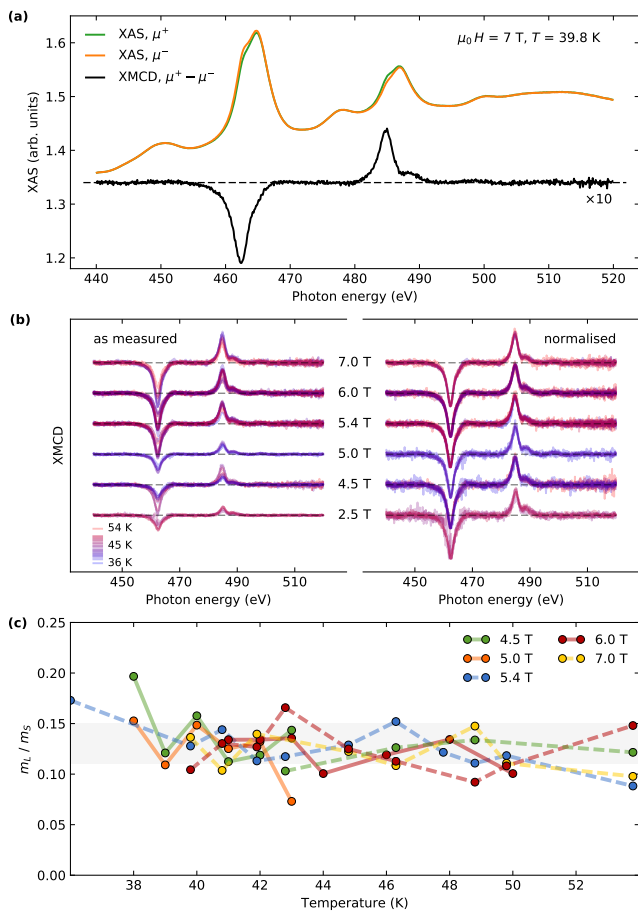
FIG. 1: (a) X-ray absorption spectra for both experimental helicities and the corresponding XMCD in the CAFM phase. (b) XMCD as a function of field and temperature in the relevant region of the phase diagram. The XMCD intensities are shown both as measured to ease comparison with macroscopic magnetization measurements (left) and normalised to average intensity to better compare the lineshapes between the XMCD spectra (right). (c) Ratio of orbital to spin moment as extracted from the XMCD data.

$R_0$ and $S_A$ (see Fig 3a). The respective intercept and slope of the linear fits to the high-field part of $\rho_{yx}$/H plotted versus $M\rho_{xx}^2$/H are listed in Table 1. Again using these materials parameters and $M(H)$ data, the Hall resistivity $\rho_{yx}$ can be *simulated* under assumption that only the normal and anomalous contributions exist. In Fig 3b we show the simulation result for T = 47 K compared to the raw data, M, $\rho_{xx}$ and $\rho_{yx}$. Both case $\alpha$=0 and 1 are shown, which correspond to an anomalous contribution dominated by intrinsic or extrinsic scattering mechanisms, respectively[5]. As can be seen from Fig 3c deviations between simulated Hall resistivity and the experimental data appear for temperatures below 49 K. This indicates the existence of a so-called topological contribution to $\rho_{yx}$ in the state corresponding to the $H - T$-region of the phase diagram, where the metamagnetic texture is observed. It may be related to either a topological contribution or another non-trivial contribution that is not considered through

normal and anomalous Hall resistivity. In particular, it may derive from effects of a non-collinear spin-structure[5].

| T | $R_0$ | $S_A$ |
|---|---|---|
| 39 | -6.4 | 2.1e-4 |
| 41 | -7.1 | 2.5e-4 |
| 43 | -6.1 | 2.7e-4 |
| 45 | -5.1 | 2.8e-4 |
| 47 | -5.2 | 3.3e-4 |
| 49 | -4.0 | 3.2e-4 |
| 51 | 0.7 | 2.2e-4 |
| 53 | 0.63 | 2.1e-4 |

TABLE I: Linear fit parameters extracted from Fig 3a.

## III.  SMALL-ANGLE NEUTRON SCATTERING MEASUREMENTS

Our SANS sample 1 measured at ILL was a 238 mg single crystal, mounted on Al sample holder with the c-axis vertical and the b-axis parallel to the field and the neutron incident momentum. The approximate sample dimensions along the major crystallographic axes were a=8.3 mm, b=7.7 mm, c=1.5 mm. The SANS sample 2 measured at PSI was a 215 mg single crystal with approximate dimensions of a=6 mm, b=5.3 mm, c=2.8 mm. The sample 2 was measured in the same orientation as sample 1. $\xi_b$, the correlation length of the magnetic texture along the *b*-axis, directed along the incident momentum of neutrons was calculated from the rocking curve measurement (rotation around the c-axis), schematically illustrated as $\omega$ rotation in Fig 4a. The rocking curve at 2 T and 48 K, obtained by rotating the sample together with a cryomagnet was fitted by a Gaussian lineshape, which yielded FWHM=3.1 and 2.7 degrees for the satellites contained in left and right boxes, Fig 4b,c.

$$\xi_b = \frac{8\ln 2}{Q\tan(b)}, \qquad (3)$$

where *b* is the full width at half maximum of the rocking curve and Q is the wavevector of the observed reflection. For estimates of $\xi_a$ and $\xi_c$, the correlation lengths along the *a* and *c* axes we used the tangential and radial widths of the satellites, which were fitted to Gaussian lineshapes. The experimental resolution in a typical SANS geometry is largely determined by the wavelength spread, $\Delta\lambda/\lambda$ and d-spacing spread of a sample, $\Delta$d/d. For the estimates of $\xi_b$ we ignored the effects of the instrumental resolution since $b >> \Theta\Delta\lambda/\lambda$ and the width of the rocking curve is much greater than the angular size of the direct beam ($\sim$0.44 degree). Here $2\Theta$ is the scattering angle.

$$\xi_a = \frac{1}{Q(\Delta d/d)}, \qquad (4)$$

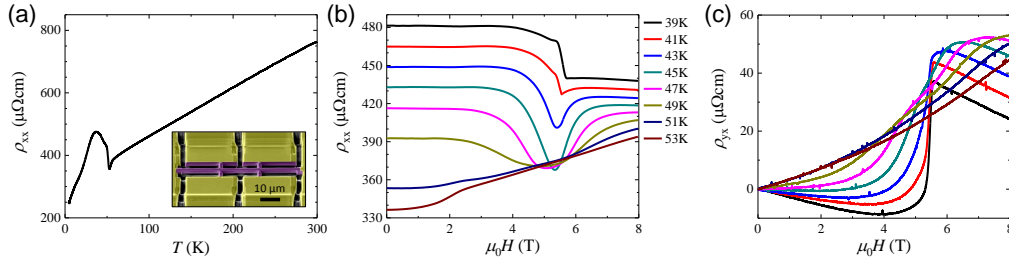where $\Delta$d/d is the d-spacing spread of the lattice, which is

FIG. 2: Transport measurements on a microstructured single crystal of $Ca_3Ru_2O_7$: (a) Temperature dependence of the in-plane resistivity. Inset: False color SEM image of the FIB-microfabricated Hall-bar device (purple) with gold contacts (yellow). Current runs along the a-axis. (b) In-plane magnetoresistivity and (c) Hall resistivity curves at various temperatures for field applied along the b-axis.
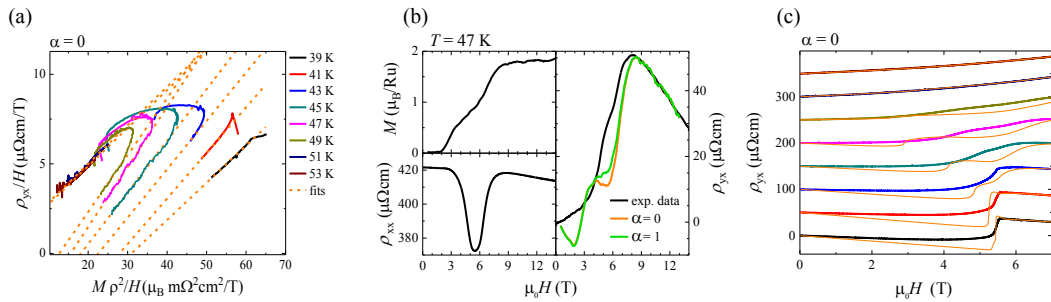


FIG. 3: (a) Linear fits (orange lines) to the Hall data from Fig 2 (c) to Eq. 2 as described in the text. The respective fit parameters we show in Table 1. (b) Example curves (black) of magnetization, in-plane resistivity and Hall resistivity, at 47 K used for fitting the Hall data according to Eq. 2. Pink and red curves are two simulations according to Eq. 2 with $\alpha$=0,1, respectively. (c) Hall resistivity data from Fig 2c, offset for better visibility. Orange curves are simulations according to Eq. 2 with $\alpha$=0 using parameters from Table 1, see text for further details.

estimated from the radial width, $R_w$ using the following,

$$(R_w/2\Theta)^2 = (a/2\Theta)^2 + (\Delta d/d)^2 + (\Delta\lambda/\lambda)^2, \quad (5)$$

where $a$ is the angular size of the direct beam as detailed in Ref.[9].

$$\xi_c = \frac{8\ln2}{Q\tan(t/2)}, \quad (6)$$

where $t$ is the intrinsic tangential variation of the lattice, which is estimated from the tangential widths of the reflection, $T_w$ and direct beam, $az$ using the following,

$$T_w = \sqrt{t^2 + az^2}, \quad (7)$$

The field dependence of $\xi_a$ and $\xi_c$ is shown in Fig 5. Whereas no clear field dependence was observed for $\xi_a$, a moderate suppression of $\xi_c$ by the field was evidenced on both instruments. In our SANS geometry the resolution in the detector plane (our $a$-, and $c$-axes) is approximately one of order of magnitude lower than along the neutron flux direction (our $b$-axis). Therefore, the values of $\xi_a$ and $\xi_c$ should be regarded as a lower limit on correlation length in the $ac$ plane.

## IV. SINGLE CRYSTAL GROWTH AND ORIENTATION OF SAMPLES

Single crystals of $Ca_3Ru_2O_7$ were grown using a floating zone method in a mirror furnace (Canon Machinery, model

SCI-MDH)), as reported elsewhere[6]. The crystal growth was performed in an atmosphere of the mixture of Ar and $O_2$ (Ar:$O_2$=85:15).

The single crystals were oriented using the X-ray Laue backscattering method utilising a home-built instrument. The typical pattern shown in Fig 6 demonstrates very sharp reflections and allows to distinguish between the $a$- and $b$-axes. The full width at the half maximum (FWHM)=0.32 degree of the rocking curve measured at the strong nuclear reflection (10 0 0) in a neutron beam with the wavelength $\lambda$=1.272 Å on D23 instrument at ILL indicated an excellent quality of our crystal, Fig 7.

Oscillation images around crystallographic axes confirm that crystal quality was maintained for the small single crystal, Fig 8.

## V. DFT CALCULATIONS

We have ascertained the presence of a sizeable effect of spin-orbit couplings (SOC) and orbital magnetic moments by standard DFT-calculations within the full-potential local orbital (FPLO) approach[10]. We used the generalized gradient approximation (GGA) as exchange-correlation functional[11]. Correlations beyond have been included by the GGA+U method for the 4d-states of Ru with an effective Hubbard-like U=0 to 3 eV. The fully relativistic FPLO code includes SOC to all orders, being based on solutions of the 4-
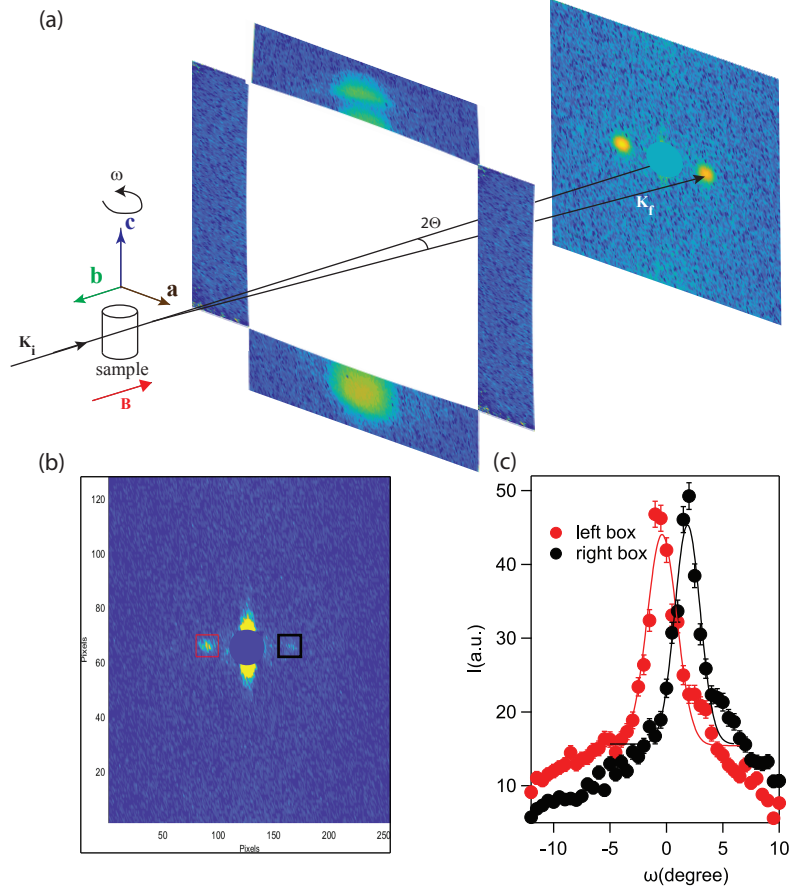
FIG. 4: (a) Geometry of SANS experiment on D33 instrument at ILL. (b) Raw SANS pattern collected at 48 K in magnetic field of 2 T. (c) Rocking scan of magnetic Bragg peaks shown in (b). Intensities in the left and right boxes in panel (b) are indicated by red and black markers, respectively. Solid lines are best fits to Gaussian lineshapes.
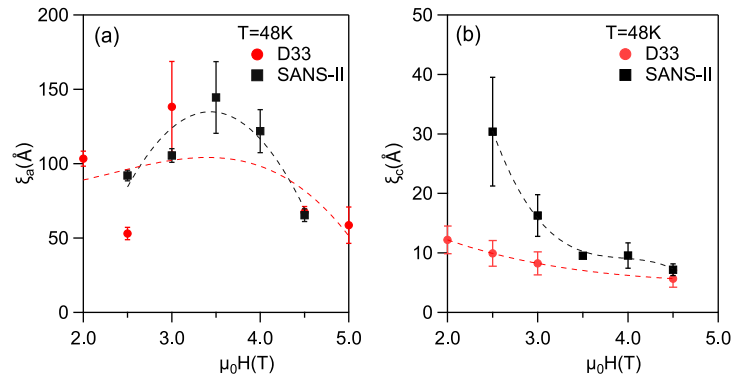


FIG. 5: Magnetic field dependence of the correlation length along the *a* (a) and *c*-axis (b) at 48 K. Dashed lines are a guide to the eye.

spinor Kohn-Sham-Dirac equations. As a relevant example, for ferromagnetic spin configurations we find spin-moments $m_s = 1.56\ \mu_B$/ Ru ion and orbital moments $m_o = 0.19\ \mu_B$/ Ru ion for a representative value of U = 2.25 eV. However, there are large uncertainties regarding exact values of spin and orbital moments, as seen from calculated results in Table II and the appropriate values for the DFT+U-correction in the metallic state at temperatures above the metal-insulator tran-

sition are uncertain. For $U \geq 3$ eV a gap opens and the band-structure would correspond to an insulating ground-state, in good agreement with earlier DFT-results by Liu[12]. However, the results indicate the presence of relatively strong SOC effects in the collinear fully polarized state. This also suggests that antisymmetric Dzyaloshinskii-Moriya exchange is relatively strong in $Ca_3Ru_2O_7$. In view of the complex bi-layer structure of $Ca_3Ru_2O_7$ and its correlated metallic character at
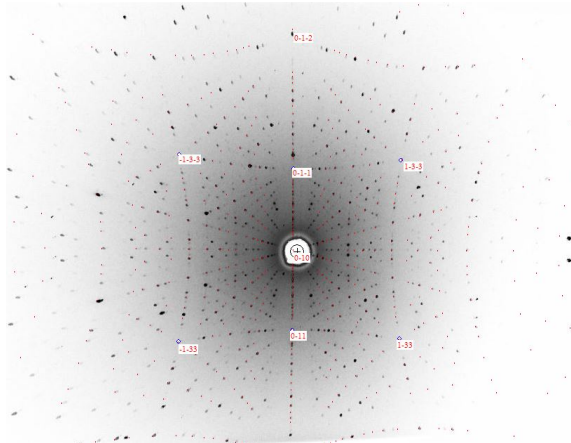
FIG. 6: The room temperature X-ray Laue diffraction pattern of an as-grown (010) facet of a $Ca_3Ru_2O_7$ single crystal. The red spots and assigned Miller indices show the calculated diffraction pattern of the Bb2$_1$m orthorhombic-space group.
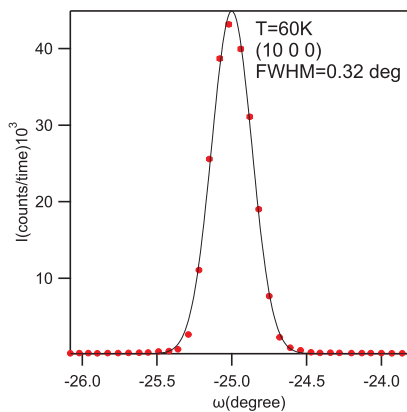


FIG. 7: The rocking curve at (10 0 0) reflection measured in a thermal neutron beam. The peak is fitted by a Gaussian lineshape with the full width at the half maximum FWHM=0.32 degree.

the relevant higher temperatures, a credible microscopic evaluation of the Dzyaloshinskii-Moriya interactions (DMIs) is hardly feasible. However, as the Ru ions occupy the general 8b Wyckoff positions in $Ca_3Ru_2O_7$, the microscopic DMIs between the spins $s_i$ on these sites, $\mathbf{D}_{ij} \cdot (\mathbf{s}_i \times \mathbf{s}_j)$ are allowed for all pairs of sites with a general Dzyaloshinksii vector $\mathbf{D}_{ij}$, which is only determined by the SOC in the spin-split electronic bandstructure.

| U | $m_s$ | $m_o$ |
| eV | $\mu_B$ / Ru | |
|---|---|---|
| 0 | 1.53 | 0.09 |
| 1.00 | 1.46 | 0.12 |
| 1.50 | 1.53 | 0.09 |
| 2.00 | 1.52 | 0.20 |
| 2.25 | 1.56 | 0.19 |
| 3.00 | 1.74 | 0.02 |

TABLE II: Magnetic spin moment $m_s$ and orbital moment $m_o$ on Ru in $Ca_3Ru_2O_7$ from GGA+U density functional theory calculations.

## VI. LANDAU-GINZBURG FREE ENERGY

The primary magnetic order in $Ca_3Ru_2O_7$ has been identified as a simple antiferromagnetic two-sublattice structure, where ferromagnetically coupled Ru-bilayers alternate with antiparallel moments stacked in $c$-direction[8]. The antiferromagnetic order breaks the B-centering operation with the vector $t = (1/2, 1/2, 0)$ (in the Cartesian coordinate system of Fig. 4 a, which will be used for spatial and spin-coordinates in the following). The metamagnetic behavior of this two-sublattice order, and the tricritical behavior Fig. 4 c, can be described by the Landau theory for the coupling of the two equivalent sublattices $\mathbf{M}_I$ and $\mathbf{M}_{II}$, but this expansion requires higher-order terms[13]. In the vicinity of the tricritical point the
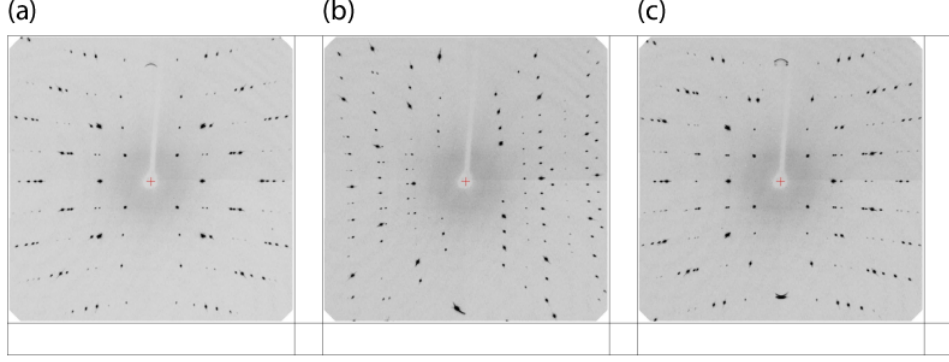
FIG. 8: (a), (b) and (c) show X-ray diffraction patterns of a small $Ca_3Ru_2O_7$ crystal after rotation about the crystallographic $a$, $b$, and $c$-axis respectively. The rotation axis in each case is vertical.

expansion can be expressed by a free energy density

$$
\begin{aligned}
F_0 &= B_2 \left( |\mathbf{M}_I|^2 + |\mathbf{M}_{II}|^2 \right) \\
&+ A_2 \mathbf{M}_I \cdot \mathbf{M}_{II} \\
&+ B_4 (|\mathbf{M}_I|^4 + |\mathbf{M}_{II}|^4) \\
&+ A_4 (\mathbf{M}_I \cdot \mathbf{M}_{II})^2 \\
&+ B_6 (|\mathbf{M}_I|^6 + |\mathbf{M}_{II}|^6) .
\end{aligned} \tag{8}
$$

$$\tag{9}$$

Representing this phenomenological theory in terms of the staggered vector $\mathbf{l} = (1/2)(\mathbf{M}_I - \mathbf{M}_{II})$ of antiferromagnetism and the net magnetic moment $\mathbf{f} = (1/2)(\mathbf{M}_I + \mathbf{M}_{II})$ leads to a free energy, which should include at least $6^{th}$ order terms in the Landau expansion to describe the tricritical point and the phase coexistence between antiferromagnetism and ferromagnetic field-enforced states,

$$
\begin{aligned}
w_0 &= a_l |\mathbf{l}|^2 + a_f |\mathbf{f}|^2 \\
&+ b_l |\mathbf{l}|^4 + b_f |\mathbf{f}|^4 \\
&+ c_1 |\mathbf{l}|^2 |\mathbf{f}|^2 \\
&+ c_l |\mathbf{l}|^6 + c_f |\mathbf{f}|^6 \\
&+ c_2 |\mathbf{l}|^4 |\mathbf{f}|^2 + c_3 |\mathbf{l}|^2 |\mathbf{f}|^4 .
\end{aligned} \tag{10}
$$

The two co-existing symmetry modes $\mathbf{l}$ and $\mathbf{f}$ and their Cartesian spin-components belong to odd and even representations of the $Cmc2_1$ space-group (which is a standard setting of space group No36 equivalent to $Bb2_1m$) with respect to the partial $t$-translation, i.e. they have different symmetry. As this crystal lattice of $Ca_3Ru_2O_7$ has a non-centrosymmetric orthorhombic symmetry belonging to Laue class 2mm, Landau-Ginzburg free energies for these two modes can have Lifshitz invariants, i.e. terms linear in spatial gradients of Cartesian components of either of these modes. These terms derive from the Dzyaloshinskii-Moriya interactions and can be written as combinations of bilinear antisymmetric forms,

$$
\Gamma_{ij}^{(\gamma)}(\mathbf{x}) \equiv (x_i \, \partial_\gamma x_j - x_j \, \partial_\gamma x_i) . \tag{11}
$$

For the 2mm symmetry and the simple antiferromagnetism

in $Ca_3Ru_2O_7$, the corresponding free energy contributions are

$$
w_D = D_x \, \Gamma_{zx}^{(x)}(\mathbf{l}) + D_y \, \Gamma_{yy}^{(y)}(\mathbf{l}) \tag{12}
$$

$$
w_F = F_x \, \Gamma_{zx}^{(x)}(\mathbf{f}) + F_y \, \Gamma_{yz}^{(y)}(\mathbf{f}) , \tag{13}
$$

where the coefficients $D_{x,y}, F_{x,y}$ are materials constants. These contributions, in particular $w_D$ lead to the spiralling cycloidal modulations of the magnetic order[14], which we call *Dzyaloshinskii textures*. In an antiferromagnet where only the $w_D$ invariants are acting, an antiferromagnetic spiral would be composed only of the l-symmetry mode. Therefore, we can refer to such a sprial as a "proper" texture. In the schematic phase diagrams, Fig.4c and Fig.4d, the presence of term $w_D$ can lead to spiralling or other precursor textures designated $\pi_1$ in particular at higher temperatures above the temperature range, where the anisotropies enforce a homogeneous antiferromagnetic state, which seems to be the case in $Ca_3Ru_2O_7$. Otherwise, the $w_D$ term can affect the antiferromagnetic order-parameter and could lead to a spiralling antiferromagnetic ground-state for weak enough anisotropies. The existence of these terms also means that the thermal phase transition from the paramagnetic to the antiferromagnetic state does not obey the Lifshitz criterion of the Landau theory for a continuous phase transition. Therefore, the thermal ordering transition in a material with a contribution of the form $w_D$ is expected to be anomalous. In particular, a fluctuating precursor states can arise above the magnetic ordering.

A complete phenomenological theory then requires also the usual squared gradient terms of the order-parameter,

$$
w_E = A_l \, (\nabla \mathbf{l})^2 + A_f \, (\nabla \mathbf{f})^2 + \dots , \tag{14}
$$

where the ellipses stand for anisotropic exchanges terms. Indeed, in $Ca_3Ru_2O_7$ strong additional anisotropies, suppress a modulation in the antiferromagnetic ground state. A complete Landau theory for the homogeneous states would require additional terms, the leading magnetocrystalline anisotropy being described by

$$
\begin{aligned}
w_a &= K_z \, l_z^2 + k_z \, f_z^2 \\
&+ \kappa_x \, l_x^2 + \kappa_{xy} \, l_x \, l_y + \kappa_y \, l_y \\
&+ \nu_x \, f_x^2 + \nu_{xy} \, l_x \, l_y + \nu_y \, l_y ,
\end{aligned} \tag{15}
$$

with anisotropy coefficients $K_z, \kappa, \nu$. We note that for doped compounds $Ca_3(Ru_{1-x}TM_x)_2O_7$, where TM is Fe or Mn, incommensurately modulated antiferromagnetic ground-states have been observed[15,16] and have been interpreted as Dzyaloshinskii spirals[17]. The observation suggests that the substituion on the magnetic site weakens the anisotropy and reveals the presence of the inhomogeneous terms $w_D$, such that the $w_D$ terms overcomes the anisotropies $w_a$.

In the region of the metamagnetic phase co-existence, additional higher order Lifshitz terms become operative, which couple $\mathbf{l}$ and $\mathbf{f}$. There are a great number improper of couplings between these modes in $Ca_3Ru_2O_7$. With the aim to illustrate the complexities of possible effects, we give here a complete list of these terms. The mixed higher order terms are Lifshitz-type invariants as follows:

$$w_\mu = \sum_{\alpha=x,y,z} \sum_{\beta=x,y} \left( a_\alpha f_\alpha^2 \Gamma_{\beta z}^{(\beta)})(\mathbf{l}) + b_\alpha l_\alpha^2 \Gamma_{\beta z}^{(\beta)}(\mathbf{m}) \right)$$ (16)

and

$$\begin{aligned}
w_\Delta =\ & \Delta_1 f_x f_y \Gamma_{xy}^{(z)}(\mathbf{l}) \\
& + \Delta_2 f_x f_y \Gamma_{zx}^{(z)}(\mathbf{l}) \\
& + \Delta_3 f_x f_y \Gamma_{yz}^{(x)}(\mathbf{l}) \\
& + \Delta_4 f_x f_y \Gamma_{yz}^{(z)}(\mathbf{l}) \\
& + \Delta_5 f_x f_y \Gamma_{zx}^{(y)}(\mathbf{l}) \\
& + \Delta_6 f_z f_x \Gamma_{xy}^{(y)}(\mathbf{l}) \\
& + \Delta_7 f_z f_x \Gamma_{zx}^{(z)}(\mathbf{l}) \\
& + \Delta_8 f_y f_z \Gamma_{xy}^{(x)}(\mathbf{l}) \\
& + \Delta_9 f_y f_z \Gamma_{yz}^{(z)}(\mathbf{l}) \\
& + \Xi_1 l_x l_y \Gamma_{xy}^{(z)}(\mathbf{f}) \\
& + \Xi_2 l_x l_y \Gamma_{zx}^{(z)}(\mathbf{f}) \\
& + \Xi_3 l_x l_y \Gamma_{yz}^{(x)}(\mathbf{f}) \\
& + \Xi_4 l_x l_y \Gamma_{yz}^{(z)}(\mathbf{f}) \\
& + \Xi_5 l_x l_y \Gamma_{zx}^{(y)}(\mathbf{f}) \\
& + \Xi_6 l_z l_x \Gamma_{xy}^{(y)}(\mathbf{f}) \\
& + \Xi_7 l_z l_x \Gamma_{zx}^{(z)}(\mathbf{f}) \\
& + \Xi_8 l_y l_z \Gamma_{xy}^{(x)}(\mathbf{f}) \\
& + \Xi_9 l_y l_z \Gamma_{yz}^{(z)}(\mathbf{l}),
\end{aligned}$$ (17)

where coefficients $\Delta$ and $\Xi$ are materials constants. When enforced by the external field or near a multicritical point, the antiferromagnetic mode $\mathbf{l}$ and $\mathbf{f}$ can co-exist, these mixed terms become operational and will allow the formation of modulated states composed of the two different modes. Therefore, we can call these modulated states "improper textures" as they are enabled by mixed terms coupling modes of diffeerent symmetry.

Aditionally, there also exist higher order Lifshitz invariants

that are quartic in either $\mathbf{l}, \mathbf{f}$

$$\begin{aligned}
w_4 =\ & \sum_{\alpha=x,y,z} \sum_{\beta=x,y} (\eta_\alpha f_\alpha^2 \Gamma_{\beta z}^{(\beta)}(\mathbf{f}) + \tau_\alpha l_\alpha^2 \Gamma_{\beta z}^{(\beta)}(\mathbf{l})) \\
& + \sigma_1 f_x f_y \Gamma_{yz}^{(x)}(\mathbf{f}) \\
& + \sigma_2 f_x f_y \Gamma_{zx}^{(y)}(\mathbf{f}) \\
& + \sigma_3 f_y f_z \Gamma_{zx}^{(y)}(\mathbf{f}) \\
& + \sigma_4 f_z f_x \Gamma_{yz}^{(x)}(\mathbf{f}) \\
& + \sigma_5 l_x l_y \Gamma_{yz}^{(x)}(\mathbf{l}) \\
& + \sigma_6 l_x l_y \Gamma_{zx}^{(y)}(\mathbf{l}) \\
& + \sigma_7 l_y l_z \Gamma_{zx}^{(y)}(\mathbf{l}) \\
& + \sigma_8 l_z l_x \Gamma_{yz}^{(x)}(\mathbf{l}).
\end{aligned}$$ (18)

Depending on many materials parameters $a_{x,yz}, b_{x,y,z}, \Delta, \Xi, \eta, \tau$, and $\sigma$, these terms describe possible coupled modulations of coexisting primary symmetry modes $\mathbf{l}, \mathbf{f}$, which can take place in distinct fashion in all three spatial directions. In addition the coupling can display markedly anharmonic effects.

We observe that the Lifshitz-(type)-invariants couple different Cartesian components of the order-parameters to different spatial directions via the gradient term. Thus, these terms break isotropy in spin-space. This implies that their microscopic origin is the relativistic spin-orbit interaction. Specifically, a microscopic mechanism to explain these terms is the antisymmetric pairwise Dzyaloshinskii-Moriya exchange, or appropriate generalization for magnetic systems with a more itinerant character of spin-ordering,

A complete Landau-Ginzburg free energy density for a polar metamagnet would collect all these terms

$$w = w_E + w_0 + w_D + w_F + w_a + w_\mu + w_\Delta + w_4 \quad (19)$$

Minimizing this free energy functional maps out all possibilities of metamagnetic modulations around a tricritical point for the specific antiferromagnetic order parameter in space group Cmc2$_1$. The corresponding Euler-Lagrange equations for the variational problem will constitute a system of coupled partial differential equations for the degrees of freedom described by the fields $\mathbf{l}(\mathbf{r})$, and $\mathbf{f}(\mathbf{r})$.

A dedicated theory for a specific material could be distilled from this most general functional by restricting to a few crucial terms. For a simple case, which may pertain to $Ca_3Ru_2O_7$, it may suffice to consider only one-dimensional modulations in $y$-direction and spin-components in the $yz$-plane. This is the case sketched in Fig.4b. The most important terms are then proper Lifshitz invariant $F_y \Gamma_{yz}^{(y)})(\mathbf{f})$ and the mixed Lifshitz-invariants $a_z f_z^2 \Gamma_{yz}^{(y)})(\mathbf{l})$ and $(b_y l_y^2 + b_z l_z^2) \Gamma_{yz}^{(y)}(\mathbf{f})$. These inhomogeneous contributions to the free energy imply that the presence of a net magnetization $f_z$ in an applied field along the polar axis favours an instability towards an antiferromagnetic modulation in the $yz$-plane. But, the local ferromagnetic modulation is also unstable with respect to modulations through the proper Lifshitz invariants.

Only strong anisotropies can prevent the instability of the spin-system towards mixed states where ferromagnetic and antiferromagnetic configurations are simultaneously present in a spatially modulated fashion. The presence of these different effective couplings then leads to modulations with a competing character, as different coupling terms co-operate and frustrate each other. In our observations, this competing character of the modulation is noticable, as the characteristic modulation length displays a pronounced temperature dependence. For an ordinary Dzyaloshinskii spiral, this behavior is unusual and unexpected[14], as in that case there is only one coupling term that rules the frustration of one simple symmetry mode. Also, the presence of the higher order term could lead to marked anharmonicities in metamagnetic textures that are driven by the higher order mixed terms.

For the particular antiferromagnetic order in $Ca_3Ru_2O_7$, the mixed Lifshitz-type terms are of higher order and affect the magnetic spin-structure only in the region of a metamagnetic co-existence. It is the underlying tricritical point which reveals the presence of these terms, Fig.4c. However, appropriate symmetry of an antiferromagnetic mode can also allow mixed Lifshitz type invariants with a bilinear form like,

$$C_{ij}^{(\gamma)} \left( f_i \, \partial_\gamma l_j - l_j \partial_\gamma f_i \right). \tag{20}$$

In the vicinity of the bi-critical point, in the case of a system with weak anisotropy, sketched in Fig. 4 d, these terms drive the existence of metamagnetic textures with modulation between antiferromagnetic ground-state in spin-flopped configuration and the field-enforced ferromagnetism.

[1] Kummer, K. *et al.* The high-field magnet endstation for X-ray magnetic dichroism experiments at ESRF soft X-ray beamline ID32. J. Synchrotron Rad. **23**, 464 (2016).

[2] Thole, B., T. *et al.* X-ray circular dichroism as a probe of orbital magnetization. Phys. Rev. Lett. **68**, 1943 (1992). Carra, P. *et al.* X-ray circular dichroism and local magnetic fields. Phys. Rev. Lett. **70**, 694 (1993). Chen, C., T. *et al.* Experimental Confirmation of the X-Ray Magnetic Circular Dichroism Sum Rules for Iron and Cobalt. Phys. Rev. Lett. **75**, 152 (1995).

[3] Kikugawa, N., Rost, A., W., Hicks, C., W., Schofield, A., J., and Mackenzie, A., P. $Ca_3Ru_2O_7$: Density Wave Formation and Quantum Oscillations in the Hall Resistivity. J. Phys. Soc. Jpn. **79(2)**, 024704 (2010).

[4] Nagaosa, N., Sinova, J., Onoda, S., MacDonald, A. H. and Ong, N. P. Anomalous Hall effect. Rev. Mod. Phys. **82**, 1539 (2010).

[5] Shiomi, Y., Iguchi, S., and Tokura, Y. Emergence of topological Hall effect from fanlike spin structure as modified by Dzyaloshinsky-Moriya interaction in MnP. Phys. Rev. B **86**, 180404(R) (2012).

[6] Perry, R., S. and Maeno, Y. Systematic approach to the growth of high-quality single crystals of $Sr_3Ru_2O_7$. J. Crystal Growth **271**, 134 (2004).

[7] Yoshida, Y., Nagai, I., Ikeda, S. I., Shirakawa, N., Kosaka, M., and Mori, N. Quasi-two-dimensional metallic ground state of $Ca_3Ru_2O_7$. Phys. Rev. B **69**, 220411(R) (2004).

[8] Yoshida Y., *et al.* Crystal and magnetic structure of $Ca_3Ru_2O_7$. Phys. Rev. B **72**, 054412 (2005).

[9] Cubitt, R., *et al.* Neutron diffraction by the flux lattice in high-T, superconductors. Physica B, **180 & 181**, 377 (1992).

[10] Koepernik, K., Eschrig, H. Full-potential nonorthogonal local-orbital minimum-basis band-structure scheme. Phys. Rev. B **59**, 1743 (1999).

[11] Perdew, J., P., Burke, K., Ernzerhof, M. Generalized gradient approximation made simple. Phys. Rev. Lett. **77**, 3865 (1996).

[12] Liu, G., Q. Mott transition and magnetic anisotropy in $Ca_3Ru_2O_7$. Phys. Rev. B, **84**, 235137 (2011).

[13] Tuszynski, J., A. Application of the Landau theory of spontaneous metamagnetism. Phys. Lett. A **85**, 175 (1981).

[14] Dzyaloshinskii, I. E. Sov. Phys. JETP **19**, 960 (1964).

[15] Ke, X., Peng, J., Tian, W., Hong, T., Zhu, M., Mao, Z. Q. Commensurate-incommensurate magnetic phase transition in the Fe-doped bilayer ruthenate $Ca_3Ru_2O_7$. Phys. Rev. B, **89**, 220407 (2014).

[16] Zhu, M., Peng, J., Tian, W., Hong, T., Mao, Z. Q and Ke, X. Tuning the competing phases of bilayer ruthenate $Ca_3Ru_2O_7$ via dilute Mn impurities and magnetic field. Phys. Rev. B **95**, 144426 (2017).

[17] Zhu, M., Hong, T., Peng, J., Zou, T., Mao, Z. Q., Ke, X. Field-induced magnetic phase transitions and memory effect in bilayer ruthenate $Ca_3Ru_2O_7$ with Fe substitution. J. Phys.: Condens. Matter **30**, 075802 (2018).